

Adaptive wavefront shaping for controlling nonlinear multimode interactions in optical fibres

Omer Tzang*, Antonio M. Caravaca-Aguirre, Kelvin Wagner and Rafael Piestun

Recent progress in wavefront shaping has enabled control of light propagation inside linear media to focus and image through scattering objects. In particular, light propagation in multimode fibres comprises complex intermodal interactions and rich spatiotemporal dynamics. Control of physical phenomena in multimode fibres and its applications are in their infancy, opening opportunities to take advantage of complex nonlinear modal dynamics. Here, we demonstrate a wavefront shaping approach for controlling nonlinear phenomena in multimode fibres. Using a spatial light modulator at the fibre input, real-time spectral feedback and a genetic algorithm optimization, we control a highly nonlinear multimode stimulated Raman scattering cascade and its interplay with four-wave mixing via a flexible implicit control on the superposition of modes coupled into the fibre. We show versatile spectrum manipulations including shifts, suppression, and enhancement of Stokes and anti-Stokes peaks. These demonstrations illustrate the power of wavefront shaping to control and optimize nonlinear wave propagation.

Controlling light propagation through complex media is key in imaging and light-energy-delivery applications¹. In the past decade, a renewed interest in the topic was sparked by new fundamental discoveries^{2,3} as well as technological improvements in devices such as spatial light modulators (SLMs) and computation capabilities. Accordingly, techniques for manipulating the wavefront incident onto the complex medium using high-resolution SLMs have helped mitigate scattering in random media⁴ and mode dispersion and coupling in multimode optical fibres (MMFs)^{5–7}. Progress in the understanding of optical nonlinear media for imaging^{8,9}, focusing through scattering layers^{10–13} and photorefractive crystals^{14,15} raises interest in fundamental nonlinear propagation and control mechanisms. While nonlinear propagation in single-mode fibres has been thoroughly investigated, only a few studies have addressed the richer nonlinear pulse propagation in MMFs, leaving this field largely unexplored with opportunities to exploit the multimodal degrees of freedom for controlling multidimensional spectral-spatiotemporal interactions^{16–19}.

Single-mode fibres have traditionally been adopted for most nonlinear applications due to the simplicity of their modal structure and propagation dynamics²⁰. However, multimode fibres are gaining new interest for communication using space-division multiplexing²¹ and high-power fibre lasers²². The higher damage threshold of large-area fibres is attractive as an alternative to power-limited single-mode fibre lasers and amplifiers²³. MMFs are important for endoscopic nonlinear microscopy and laser surgery, where nonlinear pulse distortions are expected²⁴. Recently, control over a variety of spatiotemporal nonlinear dynamics in graded-index (GRIN) MMFs has been demonstrated by manually adjusting (laterally shifting and focusing) the lens coupling to the fibre^{17,25}.

Here, we introduce wavefront shaping (WFS) to control nonlinear interactions using a SLM at the input coupling of the fibre and spectral information as feedback. Genetic algorithm optimizations tailor and optimize the highly nonlinear generation of a stimulated Raman scattering (SRS) cascade and four-wave mixing (FWM) in GRIN multimode fibres. Our methodology allows enhancement and shifting of selected Stokes or anti-Stokes (FWM) peaks by WFS optimization of the mode superposition at the fibre input. Similarly,

we show suppression of nonlinearities, which could have implications in MMF communications. The spectrum optimization provides a means to directly control nonlinear dynamics. It should be emphasized that the flexible, complex and multimode wavefront feedback control achieved with a SLM cannot be achieved with basic shifts of the laser input coupling or alignment. Hence, WFS further provides a systematic approach for controlling the complex dynamics of nonlinear phenomena in MMFs. The genetic algorithm optimization presents a solution to the inverse problem seeking to find the superposition of modes that enhances or suppresses specific nonlinear process. Remarkably, because the optimization process is implemented experimentally in the physical system, it inherently takes into account all optical system aberrations, misalignments and actual fibre configurations.

Linear WFS through fibres

Propagation of light in MMFs is described by superpositions of propagating modes. Phase-velocity mode dispersion and random mode coupling arising from imperfections and bends contribute to creating complex three-dimensional interference patterns⁷, observed as speckles at the fibre output. Lately, digital phase conjugation⁶ and WFS^{5,26} have enabled endoscopic imaging in MMFs^{6,7,24}. Spatial beam optimization in fibres with gain has been recently studied²⁷. Linear WFS techniques are based on an optimization of the input wavefront²⁶, an experimental determination of the optical transmission matrix²⁸ or direct phase conjugation⁶. In contrast to previous work, here WFS is used in the nonlinear regime where the transmission-matrix formalism is not directly applicable as linearity of the system is a basic assumption²⁸. While phase conjugation could be applied in the nonlinear regime²⁹, it does not allow explicit control of the nonlinear outcome. Even though the complex mode-coupled nonlinear propagation cannot be described by a linear superposition of modes, our genetic algorithm-based WFS strategy is appropriate as shown below.

SRS and FWM in fibres

SRS cascade generation is a nonlinear process that builds up throughout the fibre from spontaneous Raman scattering. Phase

matching for SRS is satisfied throughout the fibre as the medium is actively participating in the interaction in the sense that the process depends on lattice vibrations of the fibre. The first Stokes line builds up rapidly once the peak intensity reaches the SRS threshold, and the energy is transferred from the pump to the Stokes wave. For sufficiently large input laser pulse power, before all the energy is transferred, the Stokes wave itself serves as a pump to generate a second-order Stokes wave. If its power becomes strong enough, this process can generate a SRS cascade of multiple Stokes bands with its order increasing with fibre length²⁰. SRS cascades were demonstrated first using single-mode³⁰ and small-core³¹ fibres, and later on using large-core MMFs^{32,33} and highly customized fibres³⁴.

FWM is a χ^3 parametric nonlinear process that involves the interaction of four optical waves. Here the medium plays a catalytic role and optical momentum conservation is required for nonlinearities to build up. There are several techniques for achieving phase matching in single-mode fibres²⁰. However, in MMFs, the presence of multiple propagating modes with different dispersive properties

and momenta results in expanded phase-matching combinations for the generation of FWM signals³⁵.

The WFS control of the interplay between SRS and FWM is the major phenomenon that we explore in this study. In long fibres, SRS practically dominates the interaction because it is difficult to maintain phase matching over long fibre lengths. In shorter fibres, the phase-matching condition in MMFs can be satisfied for several combinations of the fibre modes. As such, the multimode nature of these fibres presents numerous additional opportunities for exploiting modal phase matching to enhance nonlinear interactions that remain unexplored to date.

In our experiments (Fig. 1), we launched 532 nm nanosecond pulses into a GRIN MMF. Remarkably, the SRS–FWM cascade extends from 470 nm up to 1,700 nm (the limit of our detection) and possibly beyond; with all the peaks undergoing mode cleaning (see near-field images in Fig. 1b), demonstrating that they are dominated by low-order modes rather than the typical speckle fields emerging from linear MMFs. The generated cascade is stable with fibre movement and the stability increases with fibre length. This simple MMF

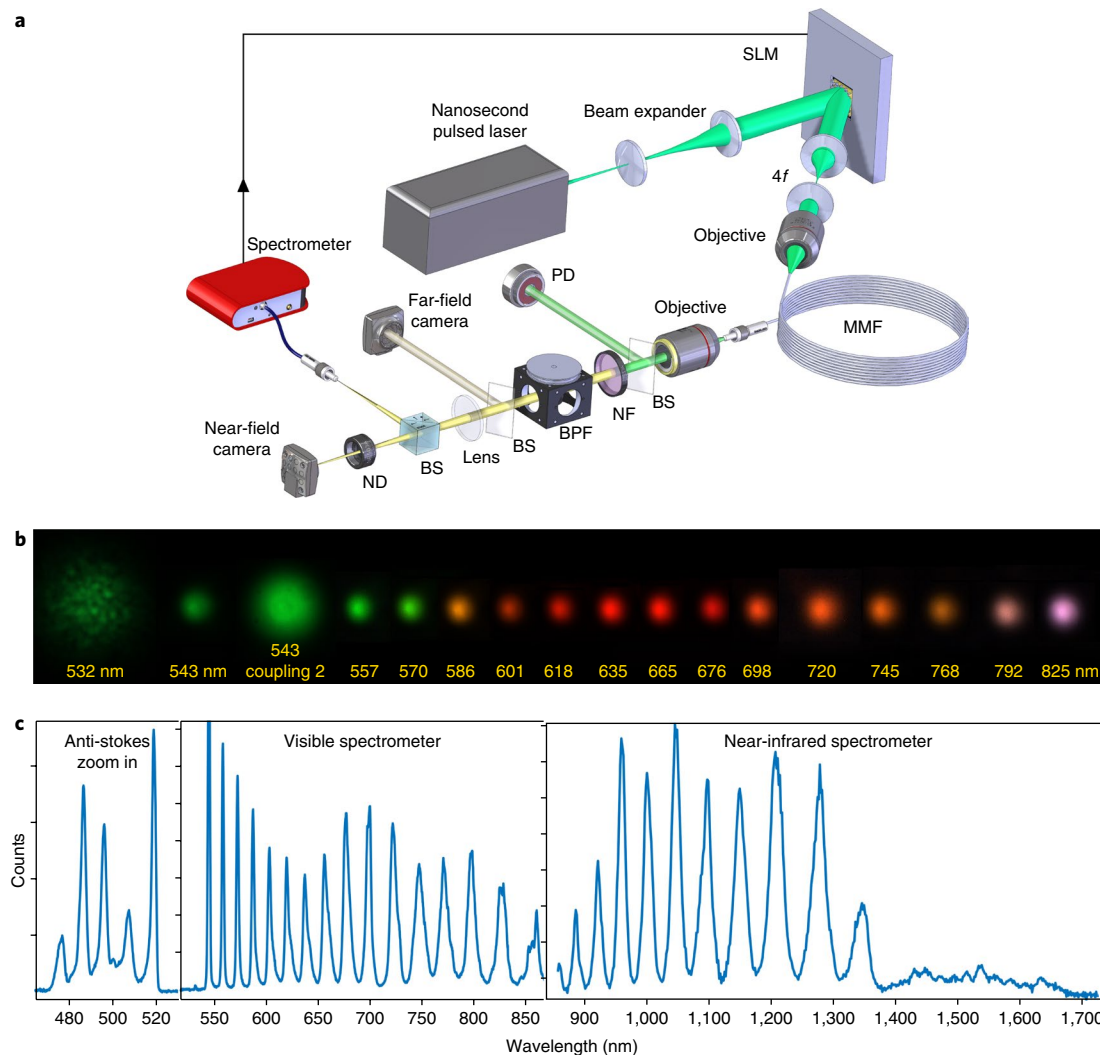


Fig. 1 | System for WFS in nonlinear multimode fibres. **a**, Optical setup (see Methods). PD, photodiode; NF, notch filter; BS, beam splitter; BPF, band-pass filter; ND, neutral density filter; 4f, afocal imaging system from SLM to fibre. **b**, Near-field imaging of SRS cascade in a MMF. Images were acquired at different filtering and camera settings, and with flat SLM phase. The 543 nm peak is depicted at two different manual couplings of the pump. **c**, Spectrum of the SRS–FWM cascade in a 1 km GRIN MMF. Anti-Stokes peaks are recorded using an additional short-pass filter. Note also the broad peak centred around 1,550 nm that may relate to modulation instability in the presence of anomalous dispersion³². The filtering and integration time in the three regions of the spectrum were varied for representation. Pulse energy $\sim 50 \mu\text{J}$; repetition rate, 20 KHz.

system produces a highly nonlinear, tunable, multiple-frequency single-mode source that is attractive for various application. In what follows, we investigate the influence of the input wavefront on the generated nonlinear phenomena.

WFS control of nonlinearities

The optical setup is depicted in Fig. 1a and described in detail in the Methods. The key components are a nanosecond laser directed to a SLM, which spatially modulates the light coupled into a MMF with $\sim 1,000$ modes, and a spectrometer that provides feedback to the computer controlling the SLM.

For WFS, we divide the SLM into independent macropixels with phases varying between 0 and 2π . A genetic algorithm optimizes the values of each macropixel based on a merit function³⁶ (see Methods). Accordingly, for each experiment, the key merit function characterizes a specific spectral feature, which is recorded at the output tip of the fibre and fed back to the computer. The genetic

algorithm process starts with a set of random phase patterns and iteratively converges to an optimized phase mask that enhances the selected spectral feature.

In what follows, we show the versatility of adaptive WFS in nonlinear fibres through several examples. In each of them, the length of the fibre was carefully chosen via cutback experiments to highlight a selected type of WFS control (Supplementary Section 7).

WFS for FWM control. In the first experiment, we investigated the enhancement of FWM interactions in short fibres, 2.65 m in this case. WFS optimizes the intensity (maximum of the peak count value) of the first FWM anti-Stokes line at 518 nm. We analysed the anti-Stokes side of the spectrum that contains only FWM peaks without the SRS peaks that dominate the Stokes side. The optimized SLM phase showed significant (sixfold) enhancement in the peak intensity compared with a flat phase at optimal mechanical focus alignment, a reference case in which the SLM serves as a mirror and

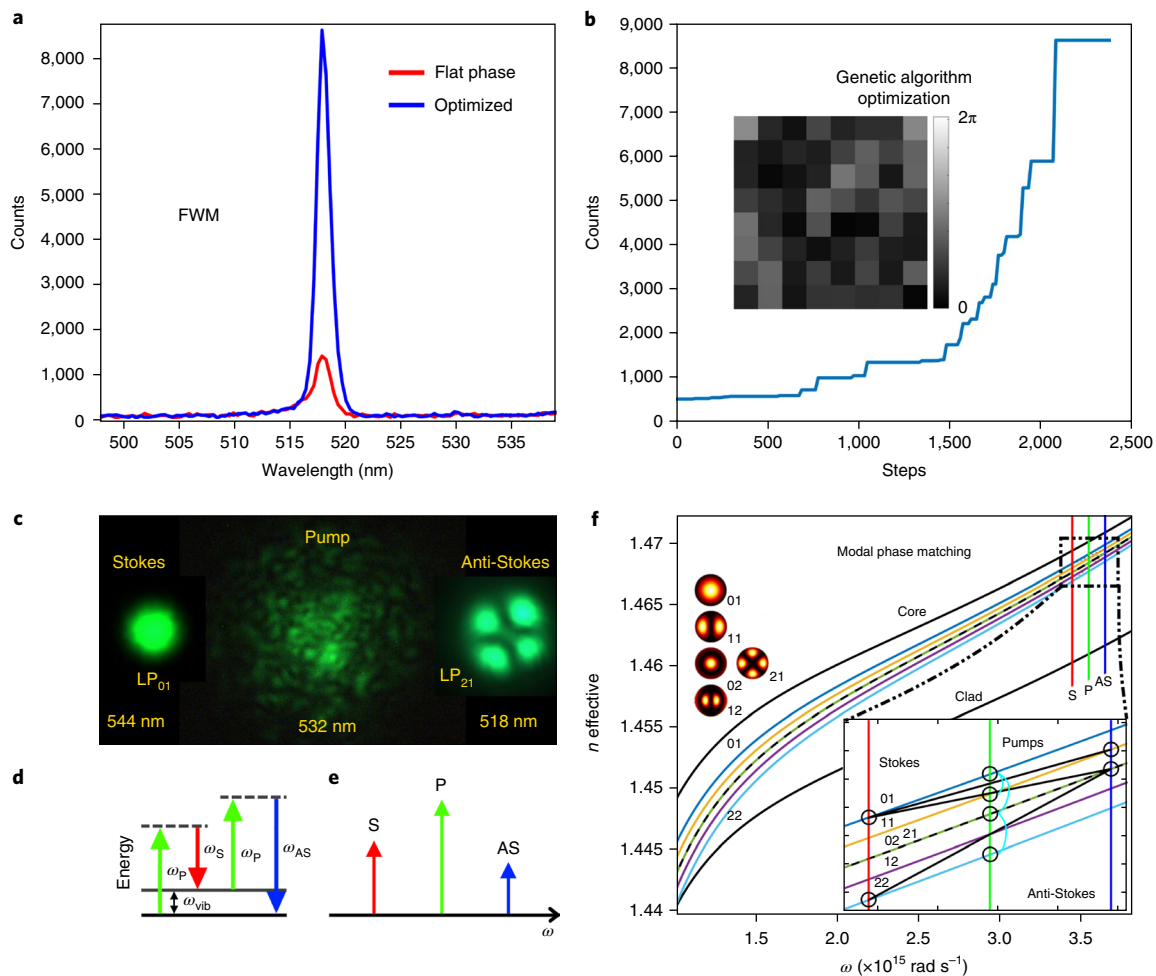


Fig. 2 | WFS of FWM. **a**, Enhancement of FWM peak at 518 nm. The 2.65 m GRIN fibre was stretched in an aluminium v-shaped-groove rail and thermally stabilized in water-based gel. **b**, Optimization process. Maximal values at each step of the genetic algorithm are depicted. The inset shows the optimal phase pattern. A 0.14 NA objective was used with a pulse energy of 32 μJ . There was no significant change in the integrated total transmission after WFS. **c**, Near-field image of the Stokes, pump and anti-Stokes peaks at the fibre output. **d**, FWM energy scheme. ω denotes the angular frequency of the four waves. **e**, FWM spectrum. **f**, Calculation of intermodal phase-matching curves. The material refractive index (n) is plotted (black) including material dispersion⁵⁴. Several modes in the GRIN fibre are shown in different colours. The bottom-right inset is zoomed-in on the experiment regime. The red, green and blue spectral lines denote Stokes (S), pump (P) and anti-Stokes (AS) wavelengths, intersecting with the calculated modes, and indicating possible propagating waves. The black lines indicate allowed phase-matched combinations. For each, we marked the two corresponding pumps with black circles and connecting light-blue curves. For each phase-matched process, the pump average falls on the crossing of the black line and pump spectral line. The top-left inset shows intensity profiles of the simulated linearly polarized (LP) modes and their indices (01, 11, 02, 21 and 12). See Supplementary Information for detailed description.

the manual coupling maximizes the peak (Fig. 2). In the comparison, the input energy was kept constant and the flat-phase spectra was measured before and after optimization to validate mechanical and thermal stability. The WFS optimization rises up sharply, at a certain threshold, reflecting the nonlinear nature of the feedback. Interestingly, the FWM anti-Stokes peak propagates as a LP₂₁ mode (Fig. 2c), completely different than the pump (highly multimode) and Stokes waves (mostly LP₀₁). Here the WFS optimization maximizes the FWM by launching a phase-matched combination of pump modes.

Intramode phase matching was first observed by Stolen et al.^{37,38} and recently regained new interest^{16,35,39,40}. Our calculations of the material refractive index of modes in GRIN fibres illustrates the mechanism of intermodal phase matching (Fig. 2f). Accordingly, the observed FWM peaks could be created by pump waves that satisfy the phase-matching condition:

$$\Delta\beta = \beta_{01}^S + \beta_{21}^{AS} - \beta_{lm}^P - \beta_{l'm'}^P \approx 0 \quad (1)$$

where $\beta_{lm}^{\text{wave}} = n_{lm}^{\text{wave}} k_0$ is the propagation constant of the mode (l, m) and $k_0 = 2\pi/\lambda$. The index ‘wave’ indicates either pump (P), Stokes (S) or anti-Stokes (AS), and λ is the wavelength. We are not operating in the pump cleaning regime¹⁹ and the optimized 532 nm pump wave is highly multimode as indicated by its speckle pattern at the output. The WFS optimization maximizes the launching of phase-matched pump modes at the input. Note that a single-mode pump at LP₀₁ cannot produce a LP₂₁ anti-Stokes with a LP₀₁ Stokes mode through a phase-matched process. Such a combination also violates angular momentum conservation. Therefore, it is evident that the pump comprises higher-order modes and, on optimization, the SLM launches efficiently a combination of phased-matched modes into the fibre, systematically surpassing what is possible with manual coupling. A detailed phase-matching model, including degeneracy splitting in GRIN, and angular momentum conservation is explored in Supplementary Sections 1–3. The mechanism for phase matching could include additional nonlinear effects, generating momenta along the GRIN fibre via self-imaging^{19,41–43} or modulation instability⁴⁴. The complexity of these nonlinear interactions highlights the advantages of WFS optimization that accounts for all the dynamically rich effects, occurring in any particular operating regime, for a desired response. Note that the injected modes might just be a means to obtain a different mode superposition at various locations down the fibre, namely the mode composition might change due to perturbation-induced coupling along propagation, and the frequency-shifted nonlinear products are accumulated throughout the fibre length.

WFS for SRS control. Next, we investigated the Stokes side of the spectrum with the goal of enhancing the SRS cascade in a 100 m GRIN fibre. The genetic algorithm optimization merit function was set for the enhancement of a selected spectral region of interest (ROI). Figure 3 depicts the SLM control over of the cascade as we selectively tune the nonlinear interaction in the MMF.

The SRS cascade can be generated in several low-order modes, as depicted in Fig. 3d. These outputs correspond to different manually coupled, multimode, off-centred, input spots. However, the most efficient cascade is generated once the pump fundamental mode is excited into the fibre, as depicted in Fig. 3a–c. In this case, the mode-cleaned pump overlaps spatially with the generated Stokes wave and the cascade keeps generating clean fundamental modes of higher wavelengths. The SLM optimizes the input superposition of modes for fundamental pump mode excitation, compensates for aberrations, mode coupling and perturbations in the optical system⁴⁵, and enables dynamic feedback monitoring on the SRS cascade.

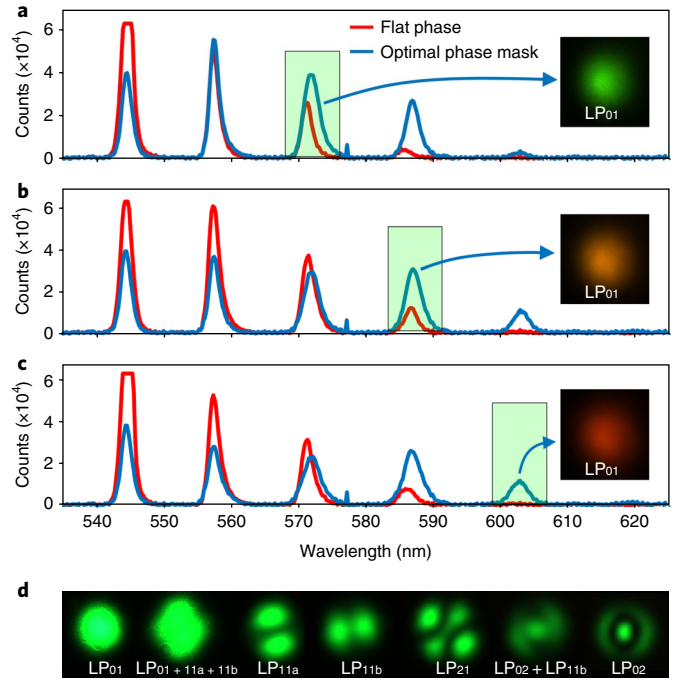


Fig. 3 | WFS of SRS peaks. **a**, Third SRS peak optimization results. The mode after WFS optimization appeared in the fundamental LP₀₁ (right inset). **b**, Fourth SRS peak optimization. **c**, Fifth SRS peak optimization. The green squares mark the spectral ROI for each optimization. In each plot, a flat phase (red) on the SLM is compared with the optimal phase mask (blue). The input energy was kept constant for comparison. A 0.14 NA objective was used with a pulse energy of 18 μJ. **d**, Near-field images of lower-efficiency, 543 nm SRS peak that were obtained with manual coupling of a focused beam in a 20 m GRIN fibre. Here the input pump is multimode and the manual coupling implicitly tunes the mode superposition and generates different Raman cleaning processes. These mode images demonstrate multimode SRS propagation.

For a discussion of physical limitations impacting the optimization see Supplementary Section 5.

WFS for spectral shift control. In terms of the modal control, the optimization of the SRS cascade efficiency is a rather simple example because it does not include complex modal excitation. In contrast, the SRS interplay with FWM illustrates more complex intermodal phase matching. Such is the case in the next experiment, depicted in Fig. 4, where we generate a SRS cascade in a 1-km-long GRIN MMF and demonstrate spectral shifting of each peak of the cascade. The spectral shifts occur as the input excitation of the fibre is continually tuned from the optimized fundamental mode (longer SRS wavelengths) to a mixed-mode excitation (SRS wavelengths downshift). At mixed modal excitation, the interplay of FWM becomes dominant and mediates the SRS cascade. For this experiment, we defined the WFS figure-of-merit function as the weighted average wavelength location in a selected spectral ROI, similar to a centre-of-mass calculation of a distribution of mass in one-dimensional space.

$$\lambda_{\text{merit}} = \pm \frac{\int_{\lambda_1}^{\lambda_2} \lambda \times I_{\text{SRS}} d\lambda}{\int_{\lambda_1}^{\lambda_2} I_{\text{SRS}} d\lambda} \quad (2)$$

where λ_1 and λ_2 define the spectral ROI, I_{SRS} is the measured spectrum intensity and \pm defines the wavelength shift direction. The

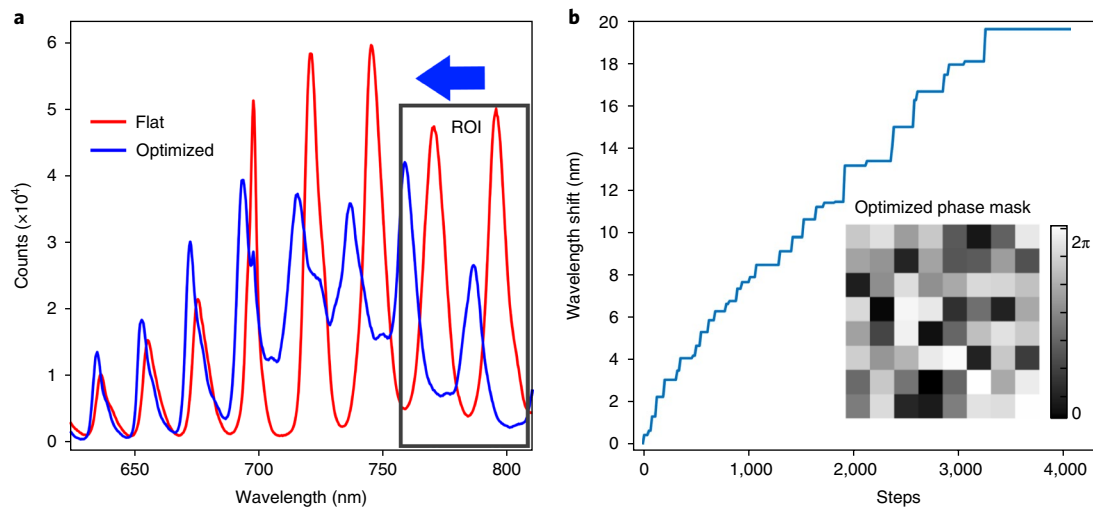


Fig. 4 | WFS of spectral shifts. **a**, Optimization of shifts towards lower wavelength and mixed-mode excitation. The genetic algorithm optimization process generated shifts of up to 20 nm. The spectrum is continually shifted with the excitation of higher-order modes that support FWM processes along the SRS cascade. The grey rectangle shows the selected spectral ROI. **b**, The genetic algorithm performance. The inset depicts the optimized phase mask. A 0.14 NA objective was used with laser pulse energy of 50 μJ . Wavelength upshift results and more details on the shifting feedback can be found in Supplementary Section 6.

SLM provides continuous control over the spectrum to produce the desired output by controlling the mixture of modes at the input of the MMF.

The spectral shifts of the cascade are obtained by mixed-mode excitation^{32,46} (Supplementary Section 6). Here, the genetic algorithm provides an optimized collection of modes on the SLM that generates a selective FWM interaction to pull the average wavelength down. Similar spectral shifts can be achieved by manually adjusting the input coupling of the fibre^{32,46}. However, the SLM provides a systematic and controlled feedback methodology that allows precise modal excitation to achieve the desired results.

WFS for SRS cascade suppression. A nonlinear tunable source based on WFS control could be beneficial for various laser applications. However, suppression of nonlinearity in MMF spatially multiplexed communication systems is desirable as these unwanted nonlinearities provide the fundamental limit to capacity^{47–50}. In Fig. 5 we demonstrate a dramatic suppression of the SRS cascade in a 1 km GRIN fibre. The suppression feedback figure of merit, F_{merit} , comprises two components: the total energy of the SRS cascade, I_{SRS} , and the total transmission in the fibre as follows:

$$F_{\text{merit}} = \frac{\int_{\lambda_1}^{\lambda_2} I_{\text{SRS (ref)}} d\lambda}{\int_{\lambda_1}^{\lambda_2} I_{\text{SRS}} d\lambda} + \frac{I_{\text{out}}}{I_{\text{out (ref)}}} \quad (3)$$

where λ_1 and λ_2 are the spectral limits of the ROI. I_{SRS} appears inverted and normalized, while I_{out} is normalized. The fibre transmission, I_{out} , is measured at the output before spectral filtering and its place in the figure of merit assures that the suppression of SRS is the result of high-mode excitation and not simply decoupling of light by diffraction on the SLM. For simplicity, we weight the two competing optimization components equally but it is possible to choose a different weighting function.

In addition, we measured the total transmission before and after optimization to normalize any diffraction effects in the suppression experiment. After optimization, the projected phase pattern decreased the total transmission by 10%, compared with an aver-

aged random phase (initial mask in the genetic algorithm process) and by 66%, compared with the flat-phase transmission. In the flat-phase comparison of Fig. 5a, we reduced the laser energy by 66%, compared with the power used in the optimization, and plotted the flat-phase output with identical total transmission to the optimized phase mask. Our optimization suppressed the SRS cascade by a factor of $\times 52$. This value represents the ratio of the integrated SRS cascade spectra for the normalized flat-phase and optimized phase cases. Figure 5b shows the WFS enhancement of the figure of merit with iteration number. The dramatic, $\times 7$, suppression of the SRS cascade from the initial random pattern shows that optimizing the higher-order mode superposition is significantly more effective than a non-optimized speckle pattern, such as could be achieved with a simple numerical aperture (NA)-matched diffuser.

Discussion

The WFS control of various nonlinear processes presented here enables spectral shaping via coupled spatial modal control. In general, as the fibres get shorter, the effect of WFS becomes more noticeable. Fibre cutback experiments show that < 50 m fibres support several SRS modes while in the longer fibres, mostly the fundamental clean mode appears, hinting that a mode competition occurs along the length of the fibre. Even with short fibres of < 5 m, the most efficient SRS cascades occur once the pump fundamental mode is excited efficiently. While similar effects could also be achieved without a SLM, using an optimized lens coupling into the fundamental mode, WFS provides a controlled way to selectively enhance the mode excitation. Furthermore, WFS enables control over FWM, spectral shifting and nonlinearities suppression by coupling a tailored superposition of modes into the fibre. All of these phenomena and capabilities are attained beyond the capabilities of simple lens coupling.

We performed numerical simulations of the nonlinear propagation with $p=8-10$ modes (see Methods and Supplementary Section 4), which showed the fundamental effects demonstrated experimentally and helped elucidate the physics behind them, albeit without the same flexibility and richness enabled by a much larger number of modes. Note, that simulation of 1,000 modes would take centuries, as the computational complexity grows exponentially

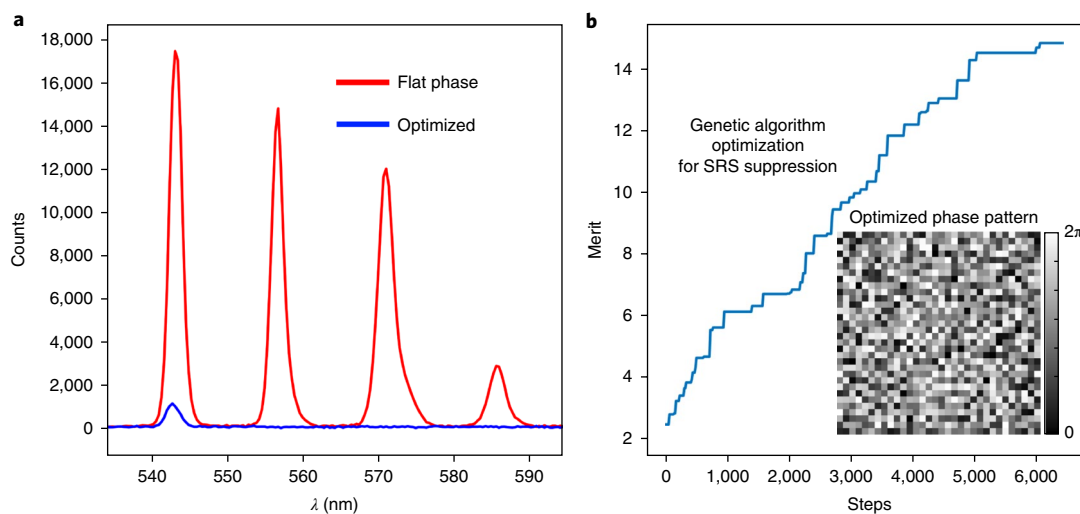


Fig. 5 | SRS cascade suppression through high-mode excitation. a, Comparison of a normalized flat phase (with 66% reduced energy) and the optimized phase spectra with matched total transmission. **b**, Performance of the genetic algorithm suppression optimization. Inset: phase mask for joint optimization of suppression through higher-order mode excitation and transmission. After optimization, the pump beam at the output was highly multimode, reflecting the high-mode propagation while the suppressed SRS appeared dominantly in the LP_{01} mode. A 0.25 NA objective was used and the pulse energy was 22.5 μ J.

as p^4 . Using a SLM and a genetic algorithm in the experiment, we controlled and optimized 1,000 modes in seconds, which shows the power of WFS in such a complex high-dimensional, nonlinear dynamical system.

The various complex processes change dramatically with fibre parameters (structure and materials), wavelength, pulse width and energy. Propagation in the fibre is further the result of random processes that are sensitive to perturbations, imperfections, initial coupling, bending and dynamic changes resulting from mechanical, thermal and material effects. For a given multimode fibre, WFS enables dynamic control of the mode superposition targeting a selected response within the fundamental limits of the particular effect. A discussion of these limitations is presented in Supplementary Section 5.

GRIN fibres have unique properties for generating interesting nonlinear interactions not always shared by step-index fibres, in particular due to differences in the variations of the modes effective area and their overlap integrals in the fibre³¹. For instance, we tested step-index fibres (50 μ m, 10 m) and could not attain SRS nor FWM with our maximal laser power in neither the experiments nor the simulations with the same power. However, both SRS and FWM were obtained with more power or thinner fibres^{37,38}. Note also that liquid-crystal SLMs and other SLMs are subject to optical damage in high-power applications. Proper precautions ensure safe operation with a high-power nanosecond laser (Supplementary Section 8).

The application of nonlinear MMFs requires long-term stability of the system. Using an active device, such as an SLM, allows a degree of dynamic control that maintains operation over long periods of time by compensating for mechanical and thermal drifts.

In moving forward and generalizing nonlinear WFS, it is interesting to explore how WFS controls systems with different types of nonlinearity. We performed our experiment in a specific regime: at a wavelength of 532 nm, normal dispersion in the fibre and utilizing nanosecond pulses, where WFS group-velocity-dispersion effects³² are of minor importance. However group-velocity differences between modes³³ could become significant in long (communication) fibres. We demonstrated several important applications of WFS control in nonlinear MMFs, and expect similar WFS methodologies to be even more significant in other systems, for instance, as femtosecond pulses in the anomalous-dispersion regime are considered.

Conclusion

We presented WFS control and optimization of nonlinear interactions in MMFs. By optimizing the input phase of the fibre-coupled wavefront, we tuned the energy of selected SRS and FWM peaks creating a configurable source with tailored performance. The adaptive in-line optimization represents an approach to solve the nonlinear inverse problem of finding a tailored superposition of modes at the input of the fibre for a desired spectral output, a problem that cannot be solved with current computation technology due to its complexity. This work opens opportunities for characterizing and controlling rich spatiotemporal dynamics in MMFs. Its potential applications include nonlinear frequency generation, high-power MMF lasers, nonlinear endoscopy and nonlinearity suppression in multimode fibres.

Methods

Methods, including statements of data availability and any associated accession codes and references, are available at <https://doi.org/10.1038/s41566-018-0167-7>.

Received: 26 June 2017; Accepted: 6 April 2018;

Published online: 7 May 2018

References

- Mosk, A. P., Lagendijk, A., Lerosey, G. & Fink, M. Controlling waves in space and time for imaging and focusing in complex media. *Nat. Photon.* **6**, 283–292 (2012).
- Vellekoop, I. M. & Mosk, A. P. Focusing coherent light through opaque strongly scattering media. *Opt. Lett.* **32**, 2309–2311 (2007).
- Katz, O., Small, E. & Silberberg, Y. Looking around corners and through thin turbid layers in real time with scattered incoherent light. *Nat. Photon.* **6**, 549–553 (2012).
- Park, J.-H., Sun, W. & Cui, M. High-resolution in vivo imaging of mouse brain through the intact skull. *Proc. Natl Acad. Sci. USA* **112**, 9236–9241 (2015).
- Čížmár, T. & Dholakia, K. Exploiting multimode waveguides for pure fibre-based imaging. *Nat. Commun.* **3**, 1027 (2012).
- Papadopoulos, I. N., Farahi, S., Moser, C. & Psaltis, D. High-resolution, lensless endoscope based on digital scanning through a multimode optical fiber. *Biomed. Opt. Express* **4**, 260–270 (2013).
- Caravaca-Aguirre, A. M., Niv, E., Conkey, D. B. & Piestun, R. Real-time resilient focusing through a bending multimode fiber. *Opt. Express* **21**, 12881–12887 (2013).
- Barsi, C., Wan, W. & Fleischer, J. W. Imaging through nonlinear media using digital holography. *Nat. Photon.* **3**, 211–215 (2009).

9. Masihzadeh, O., Schlup, P. & Bartels, R. A. Enhanced spatial resolution in third-harmonic microscopy through polarization switching. *Opt. Lett.* **34**, 1240–1242 (2009).
10. Katz, O., Small, E., Guan, Y. & Silberberg, Y. Noninvasive nonlinear imaging through strongly-scattering turbid layers. *Optica*. **1**, 170–174 (2014).
11. Tzang, O. & Piestun, R. Lock-in detection of photoacoustic feedback signal for focusing through scattering media using wave-front shaping. *Opt. Express* **24**, 28122–28130 (2016).
12. Frostig, H. et al. Focusing light by wavefront shaping through disorder and nonlinearity. *Optica* **4**, 1073–1079 (2017).
13. Qiao, Y., Peng, Y., Zheng, Y., Ye, F. & Chen, X. Second-harmonic focusing by nonlinear turbid medium via feedback-based wavefront shaping. *Opt. Lett.* **42**, 1895–1898 (2017).
14. Cohen, O. et al. Observation of random-phase lattice solitons. *Nature* **433**, 500–503 (2005).
15. Sun, C., Waller, L., Dylov, D. V. & Fleischer, J. W. Spectral dynamics of spatially incoherent modulation instability. *Phys. Rev. Lett.* **108**, 263902 (2012).
16. Demas, J. et al. Intermodal nonlinear mixing with Bessel beams in optical fiber. *Optica* **2**, 14–17 (2015).
17. Wright, L. G., Christodoulides, D. N. & Wise, F. W. Controllable spatiotemporal nonlinear effects in multimode fibres. *Nat. Photon.* **9**, 306–310 (2015).
18. Wright, L. G. et al. Self-organized instability in graded-index multimode fibres. *Nat. Photon.* **10**, 771–776 (2016).
19. Krupa, K. et al. Spatial beam self-cleaning in multimode fiber. *Nat. Photon.* **11**, 237–241 (2017).
20. Agrawal, G. P. *Nonlinear Fiber Optics* 4th edn (Academic Press, 2007).
21. Li, G., Bai, N., Zhao, N. & Xia, C. Space-division multiplexing: the next frontier in optical communication. *Adv. Opt. Photon.* **6**, 293–339 (2014).
22. Gong, M. et al. Numerical modeling of transverse mode competition in strongly pumped multimode fiber lasers and amplifiers. *Opt. Express* **15**, 3236–3246 (2007).
23. Richardson, D. J., Nilsson, J. & Clarkson, W. A. High power fiber lasers: current status and future perspectives. *Josa B* **27**, B63–B92 (2010).
24. Caravaca-Aguirre, A. M. & Piestun, R. Single multimode fiber endoscope. *Opt. Express* **25**, 1656–1665 (2017).
25. Wright, L. G., Renninger, W. H., Christodoulides, D. N. & Wise, F. W. Spatiotemporal dynamics of multimode optical solitons. *Opt. Express* **23**, 3492–3506 (2015).
26. Choi, Y. et al. Scanner-free and wide-field endoscopic imaging by using a single multimode optical fiber. *Phys. Rev. Lett.* **109**, 203901 (2012).
27. Florentin, R. et al. Shaping the light amplified in a multimode fiber. *Light Sci. Appl.* **6**, e16208 (2017).
28. Popoff, S. M. et al. Measuring the transmission matrix in optics: an approach to the study and control of light propagation in disordered media. *Phys. Rev. Lett.* **104**, 100601 (2010).
29. Bowers, M. W., Boyd, R. W. & Hankla, A. K. Brillouin-enhanced four-wave-mixing vector phase-conjugate mirror with beam-combining capability. *Opt. Lett.* **22**, 360–362 (1997).
30. Stolen, R. H., Ippen, E. P. & Tynes, A. R. Raman oscillation in glass optical waveguide. *Appl. Phys. Lett.* **20**, 62–64 (1972).
31. Rosman, G. High-order comb spectrum from stimulated Raman scattering in a silica-core fibre. *Opt. Quantum Electron. Electron.* **14**, 92–93 (1982).
32. Pourbeyram, H., Agrawal, G. P. & Mafi, A. Stimulated Raman scattering cascade spanning the wavelength range of 523 to 1750 nm using a graded-index multimode optical fiber. *Appl. Phys. Lett.* **102**, 1–5 (2013).
33. Chiang, K. S. Stimulated Raman scattering in a multimode optical fiber: self-focusing or mode competition? *Opt. Commun.* **95**, 235–238 (1993).
34. Couny, F., Benabid, F., Roberts, P. J., Light, P. S. & Raymer, M. G. Generation and photonic guidance of multi-octave optical-frequency combs. *Science* **318**, 1118–1121 (2007).
35. Nazemosadat, E., Pourbeyram, H. & Mafi, A. Phase matching for spontaneous frequency conversion via four-wave mixing in graded-index multimode optical fibers. *J. Opt. Soc. Am. B* **33**, 144–150 (2016).
36. Conkey, D. B., Brown, A. N., Caravaca-Aguirre, A. M. & Piestun, R. Genetic algorithm optimization for focusing through turbid media in noisy environments. *Opt. Express* **20**, 4840–4849 (2012).
37. Stolen, R. H., Bjorkholm, J. E. & Ashkin, A. Phase-matched three-wave mixing in silica fiber optical waveguides. *Appl. Phys. Lett.* **24**, 308–310 (1974).
38. Stolen, R. H. Phase-matched-stimulated four-photon mixing in silica-fiber wave. *IEEE J. Quantum Electron.* **11**, 100–103 (1975).
39. Pourbeyram, H. & Mafi, A. Photon pair generation in multimode optical fibers via intermodal phase matching. *Phys. Rev. A* **94**, 023815 (2016).
40. Upiol, R. D. et al. Far-detuned cascaded intermodal four-wave mixing in a multimode fiber. *Opt. Lett.* **42**, 1293–1296 (2017).
41. Wright, L. G., Wabnitz, S., Christodoulides, D. N. & Wise, F. W. Ultrabroadband dispersive radiation by spatiotemporal oscillation of multimode waves. *Phys. Rev. Lett.* **115**, 223902 (2015).
42. Krupa, K. et al. Observation of geometric parametric instability induced by the periodic spatial self-imaging of multimode waves. *Phys. Rev. Lett.* **116**, 183901 (2016).
43. Pourbeyram, H. & Mafi, A. Apparent non-conservation of momentum of light due to strongly coupled nonlinear dynamics in a multimode optical fiber. Preprint at <https://arxiv.org/abs/1701.05606> (2017).
44. Dupiol, R. et al. Intermodal modulational instability in graded-index multimode optical fibers. *Opt. Lett.* **42**, 3419–3422 (2017).
45. Lombard, L., Brignon, A., Huignard, J. P., Lallier, E. & Georges, P. Beam cleanup in a self-aligned gradient-index Brillouin cavity for high-power multimode fiber amplifiers. *Opt. Lett.* **31**, 158–160 (2006).
46. Sharma, A., Dokhanian, M., Wu, Z., Williams, A. & Venkateswarlu, P. Four-photon-mixing-mediated stimulated Raman scattering in a multimode optical fiber. *Opt. Lett.* **19**, 1122–1124 (1994).
47. Temprana, E. et al. Overcoming Kerr-induced capacity limit in optical fiber transmission. *Science* **348**, 1445–1448 (2015).
48. Mitra, P. P. & Stark, J. B. Nonlinear limits to the information capacity of optical fibre communications. *Nature* **411**, 1027–1030 (2001).
49. Essiambre, R., Kramer, G., Winzer, P. J., Foschini, G. J. & Goebel, B. Capacity limits of optical fiber networks. *J. Light. Technol.* **28**, 662–701 (2010).
50. Chraplyvy, A. R. Limitations on lightwave communications imposed by optical-fiber nonlinearities. *J. Light. Technol.* **8**, 1548–1557 (1990).
51. Terry, N. B., Alley, T. G., Russell, T. H. & Engel, K. T. An explanation of SRS beam cleanup in graded-index fibers and the absence of SRS beam cleanup in step-index fibers. *Opt. Express* **15**, 17509–17519 (2007).
52. Katz, O., Small, E., Bromberg, Y. & Silberberg, Y. Focusing and compression of ultrashort pulses through scattering media. *Nat. Photon.* **5**, 372–377 (2011).
53. Shen, X., Kahn, J. M. & Horowitz, M. A. Compensation for multimode fiber dispersion by adaptive optics. *Opt. Lett.* **30**, 2985–2987 (2005).
54. Shibata, N., Shibata, S. & Eda, H. Refractive index dispersion of lightguide glasses at high temperature. *Electron. Lett.* **17**, 310–311 (1981).

Acknowledgements

We thank F. Wise, L. Wright and R. Ulbricht for fruitful discussions. We thank S. Singh for help with the mode simulations. We acknowledge support from the National Science Foundation through awards 1611513 and 1548924, and from the National Institute of Health award REY026436A.

Author contributions

O.T., A.M.C.-A. and R.P. initiated the project. A.M.C.-A. and O.T. performed the SRS enhancement experiments. O.T. designed and performed the FWM and suppression experiments. K.W. and O.T. performed the intermodal phase-matching analysis. O.T. and A.M.C.-A. performed the numerical simulations. R.P. provided overall supervision. O.T. wrote the first version of the manuscript. All authors were involved in the analysis of the results and revision of the manuscript.

Competing interests

The authors declare no competing interests.

Additional information

Supplementary information is available for this paper at <https://doi.org/10.1038/s41566-018-0167-7>.

Reprints and permissions information is available at www.nature.com/reprints.

Correspondence and requests for materials should be addressed to O.T.

Publisher's note: Springer Nature remains neutral with regard to jurisdictional claims in published maps and institutional affiliations.

Methods

Experimental setup. The optical setup used in the experiment is depicted in Fig. 1a. It includes a laser source (Spectra Physics, Mosaic) with 532 nm, ~7 ns pulses, energy up to 150 μ J and repetition rate of 20 KHz. WFS was performed using a liquid-crystal SLM (Meadowlark 512 \times 512). Reflected light of the SLM was imaged by a 4f system onto the back aperture of a microscope objective (Olympus, 0.14 NA or Leica 0.25 NA) that couples the light into the MMF. We used an off-the-shelf GRIN fibre (Corning, 62.5/125 μ m) with changing lengths in the range of 2.65 m–1 km. For the SRS enhancement experiments (Fig. 3a–c), we used a 100 m, 62.5/125 μ m fibre (Thorlabs GIF625). Step-index fibre (Thorlabs FG050LGA) was used as well. The fibre output was coupled into a customized microscope for near and far-field imaging of fibre modes with the possibility to switch between different optical configurations. The microscope includes output power monitoring, notch filter (Thorlabs NF533-17), tunable neutral density filter attenuation and a series of narrow band-pass filters. The anti-Stokes bands were analysed using a short-pass filter (Semrock BPS01-532-25) to avoid saturation of the detector due to the intense SRS. For parallel spectral detection, the light beam was split and coupled into a MMF to average the spectrum in space and from there coupled into a spectrometer (OceanOptics Flame VIS-NIR or NIR-512). The signal from the spectrometer was acquired and analysed by a computer.

Thermal management plays an interesting role in the SRS cascade. To eliminate thermal effects in the FWM experiment, we aligned a short fibre in an aluminium v-shaped profile and immersed the fibre in water-based gel. The configuration, suitable only for short fibres, provided improved thermal management and produced far better reproducibility of the nonlinear optimization algorithm. We compared the flat-phase spectrum before and after optimization to ensure that the thermal management keeps the fibre at the same conditions over time and during WFS.

For WFS, we divide the SLM into independent macropixels whose phase varies between 0 and 2π . The number of macropixels utilized in the SLM has to be carefully considered. Once phase patterns are displayed, some of the light is diffracted out of the fibre, reducing the coupled input power and decreasing the nonlinearity regardless of the particular modes excited. As the number of SLM macropixels increases, the diffraction spectrum broadens, further reducing the input power coupled into the fibre. Therefore, the number of SLM macropixels was limited between 64 and 1,024, and each 512 \times 512 phase pattern is convolved with a circular kernel of 2–5 SLM pixels to smooth the phase edges. This step avoids diffraction at large angles that miss that fibre and produces a better mode matching with the fibre. We took these effects into account and presented our results with strict criteria, namely a constant laser power for enhancement and a normalized coupling power into the fibre for suppression, as described above. A genetic algorithm optimized the values of each macropixel based on a merit function tailored to the experiment, as shown in Supplementary Movies 1–3.

Genetic algorithms. The genetic algorithm optimization for WFS^{36,55} starts with a population set of random phase masks (30 in our case) and iteratively converges to an optimized pattern. At each step, a phase mask is displayed on the SLM and a merit signal is recorded, based on a specified spectral analysis at the fibre output.

The recorded values of the initial population are ranked based on the selected figure of merit, the best is kept, and a new generation, containing new phase masks (15 off-springs in our case), is created. The breeding process combines two phase masks, which are selected from the population with a probability weighted by the ranking, through breeding and mutation operations. At each step of the genetic algorithm, a new phase mask is displayed on the SLM and the corresponding figure of merit is recorded. The ranking and breeding process repeats itself every cycle (15 measurements in our case), always keeping the 30 highest-ranked phase masks as the population for the next iteration. As a result, a phase mask is found that enhances the selected figure of merit and corresponding spectral feature. The optimization time is determined by the number of steps and the acquisition time. Typically, the spectrometer acquisition time is set to 10 ms with additional $\times 3$ averaging for each step. The SLM refresh time is also in the order of 10 ms leading to approximately 50 ms per measurement. Accordingly, for ~10,000 measurements, the optimization times were in the order of 10 min using a non-optimized MATLAB software. The main advantage of the genetic algorithm over other optimization algorithms is its performance in the presence of noise³⁶, and its flexibility to utilize various feedback mechanisms. In the genetic algorithm results, we plot the best value of each iteration consisting of N steps, with N being the number of new phase masks in the population. It is characteristic for a random search genetic algorithm optimization that during several cycles, there is little or no improvement, namely the best element of the new generation is not better than the best of the previous one. Therefore, our plots show a staircase-like shape where a no-improvement iteration is a straight line in length of $N=15$ steps. Note that the algorithm operations (mutation and crossover) are not a local search, like gradient descent, so incremental steps are not the only behaviour to be expected in the genetic algorithm. Algorithm parameters, such as the mutation rate and mutation decay rate, influence the optimization. We set these parameters empirically for optimal performance and keep them constant throughout the experiments.

Simulations. Modal phase-matching curves were calculated using mode solvers and beam propagation techniques (ADL and MATLAB). Simulations to illustrate the experiments were performed using the generalized multimode nonlinear Schrödinger equation, implemented with a numerical solver in MATLAB⁵⁶ (Supplementary Section 4). A simulation of 8–10 modes in a 10 m fibre takes about 6 h, using a state-of-the-art parallel graphics processing unit implementation.

Data availability. The data used in this paper are available from the corresponding author upon request.

References

55. Tzang, O., Niv, E., Caravaca-Aguirre, A. M. & Piestun, R. Thermal expansion feedback for wave-front shaping. *Opt. Express* **25**, 6122–6131 (2017).
56. Wright, L. G. et al. Multimode nonlinear fiber optics: massively parallel numerical solver, tutorial and outlook. *IEEE J. Sel. Top. Quantum Electron.* **24**, 5100516 (2018).